Level shifts of rubidium Rydberg states due to binary interactions

A. Reinhard, T. Cubel Liebisch, B. Knuffman, and G. Raithel
FOCUS Center and Michigan Center for Theoretical Physics, Department of Physics, University of Michigan, Ann Arbor, Michigan 48109, USA

(Received 16 August 2006; published 14 March 2007; corrected 19 March 2007)

We use perturbation theory to directly calculate the van der Waals and dipole-dipole energy shifts of pairs of interacting Rb Rydberg atoms for different quantum numbers n, ℓ, j, and m_j, taking into account a large number of perturbing states. Our results can be used to identify good experimental parameters and illuminate important considerations for applications of the "Rydberg-excitation blockade." We also use the results of the calculation to explain features of previous experimental data on the Rydberg-excitation blockade. To explore control methods for the blockade, we discuss energy shifts due to atom-atom interaction in an external electric field.

DOI: 10.1103/PhysRevA.75.032712 PACS number(s): 34.20.Cf, 31.15.Md, 34.60.+z, 03.67.−a

I. INTRODUCTION

Due to their large sizes and polarizabilities, Rydberg atoms excited from ensembles of laser-cooled ground state atoms interact strongly via resonant dipole-dipole or off-resonant van der Waals interactions. These interactions can lead to a number of interesting collisional effects including state mixing [1,2], the formation of ultracold plasmas [3–5], and the conversion of internal energy to center-of-mass energy [6,7]. For relatively low densities and short interaction times, however, a window of experimental parameters exists in which these incoherent processes are sufficiently suppressed so that fragile, coherent dynamics is observable. A coherent phenomenon that has recently attracted attention is the so-called "Rydberg-excitation blockade," or "Rydberg blockade." If a small atomic sample is uniformly excited into Rydberg levels, collective states are created in which Rydberg excitations are coherently shared among all atoms. For example, the first excited state of an N-atom ensemble is $|N,1\rangle=(1/\sqrt{N})\Sigma_{i=1}^{N}|g_1,g_2,\ldots,r_i,\ldots,g_N\rangle$, where the subscripts are the atom labels and $|g\rangle$ and $|r\rangle$ denote an atom in the ground state and the Rydberg state, respectively. The energy levels of the system deviate from an equally spaced ladder of energies because of coherent interactions between Rydberg atoms. This is schematically represented in Fig. 1. The energy of the second excited state, $|N,2\rangle$, is shifted by the interaction energy, V_{Int}, from its interaction-free value. If the laser is tuned to the lowest transition in the system $|N,0\rangle\rightarrow|N,1\rangle$ and has a frequency bandwidth less than V_{Int}/h, excitation of all quantum states higher in energy than $|N,1\rangle$ is suppressed. This "blockade" of higher excitations can potentially be applied to quantum information processing [8,9], quantum cryptography [10], atomic clocks [11], the generation of mesoscopic entanglement [8], and the improvement of spectroscopic resolution [8].

Significant progress has been made towards demonstrating and understanding the blockade. Evidence of the blockade effect has been observed in the suppression of bulk Rydberg excitation in large samples [12,13] and in the counting statistics of the number of Rydberg excitations in small Rydberg-atom samples [14]. Experimental evidence of a blockade realized by the tuning of a Förster resonance in an external electric field has also been reported [15]. The Rydberg blockade has been modeled using many-body quantum simulations [16,17], and the application of the blockade to quantum phase gates [18,19] has been analyzed. Additional work has been done to characterize Rydberg-atom interactions, including spectroscopic studies of resonant dipolar interactions [5,20,21], observation and characterization of molecular resonances [22,23], and a study of the angular dependence of dipolar Rydberg atom interactions [24].

In Refs. [12–14,16,17], the Rydberg blockade is based primarily on level shifts caused by binary interactions between Rydberg excitations. While it is straightforward to estimate the order of magnitude of such interactions, knowledge of their detailed dependence on the atomic species, quantum numbers, interatomic separations, etc., is important to understand the exact behavior of systems of interacting Rydberg atoms. In this paper, we present calculations of van der Waals and dipole-dipole energy level shifts, V_{Int}, of pairs of Rb Rydberg atoms for different quantum numbers n, ℓ, j, and m_j, accounting for a large number of perturbing states. We identify parameter ranges suitable for applications of the Rydberg blockade and explain some features of recent experimental data [14]. We then discuss mechanisms for control of the Rydberg blockade based on calculations of interaction energies in external electric fields. These control schemes may become useful in the proposed applications discussed above.

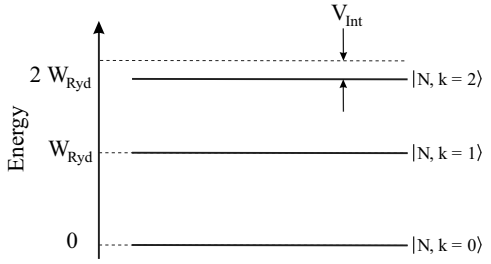

FIG. 1. Lowest collective states of an ensemble of N atoms containing k Rydberg excitations. Binary Rydberg-Rydberg interaction causes an energy shift V_{Int} of the state $|N,k=2\rangle$.

II. COMPUTATION OF BINARY-INTERACTION LEVEL SHIFTS

We use perturbation theory to compute the second-order, binary interaction-induced energy level shifts due to couplings of the type $\langle B|\otimes\langle C|V_{\mathrm{Int}}|A\rangle\otimes|A\rangle$, where $|A\rangle$, $|B\rangle$, and $|C\rangle$ are single-particle Rydberg states. Generally, the interaction operator, V_{Int}, can be expanded in multipole terms that scale with increasing negative powers of the interatomic separation, R [25–27]. This paper primarily addresses situations in which the typical Rydberg-atom separation, R, is about an order of magnitude larger than the atom size (Refs. [12–14,16,17]). In first order, the electric-dipole interaction scales as $V_{\mathrm{Int}}\sim n^4/R^3$. If there is no external electric field applied, the electric-dipole interaction produces level shifts only in second order, because low-angular-momentum Rydberg states of alkali atoms in zero electric field do not have permanent dipole moments. For this case, the level shifts scale as $\sim n^{11}/(sR^6)$, where the parameter s is a measure for the magnitude of the energy detunings that occur in second-order perturbation theory and is of order 0.1 or less [5]. For P and D states, the quadrupole-quadrupole interaction occurs in first order and leads to shifts that scale as $\sim n^8/R^5$. The ratio of the quadrupole-quadrupole interaction to the second-order dipole-dipole interaction scales as sR/n^3. For the interatomic separations of interest in this paper ($R\sim 10n^2$), this ratio is $\sim 1/n$. We therefore restrict our calculations to the dipole-dipole interaction, which represents the dominant interaction at the atomic separations of interest. It is noted that in more general cases quadrupolar and higher interactions will also become important [25–29].

In the case of zero external field, computation of the van der Waals level shifts due to the electric-dipole interaction requires the evaluation of matrix elements of the form $\langle n'',\ell'',j'',m_j''|\otimes\langle n',\ell',j',m_j'|V_{dd}|n,\ell,j,m_j\rangle\otimes|n,\ell,j,m_j\rangle$, where V_{dd} is the potential energy operator for two interacting electric dipoles. The operator V_{dd} is given, in atomic units, by

$$V_{dd}=\frac{\mathbf{p}_1\cdot\mathbf{p}_2-3(\mathbf{n}\cdot\mathbf{p}_1)(\mathbf{n}\cdot\mathbf{p}_2)}{R^3}, \tag{1}$$

where the operators $\mathbf{p}_1$ and $\mathbf{p}_2$ denote the individual electric-dipole moments, the vector $\mathbf{R}$ is the separation between the classical center-of-mass coordinates of the interacting atoms, and $\mathbf{n}$ is a unit vector pointing in the direction of $\mathbf{R}$. The geometry of the problem is depicted in Fig. 2.

V_{dd} can be written as

$$V_{dd}=\frac{p_{1x}p_{2x}(1-3\sin^2\theta)+p_{1y}p_{2y}+p_{1z}p_{2z}(1-3\cos^2\theta)}{R^3}-\frac{3\sin\theta\cos\theta(p_{1x}p_{2z}+p_{1z}p_{2x})}{R^3}$$

or

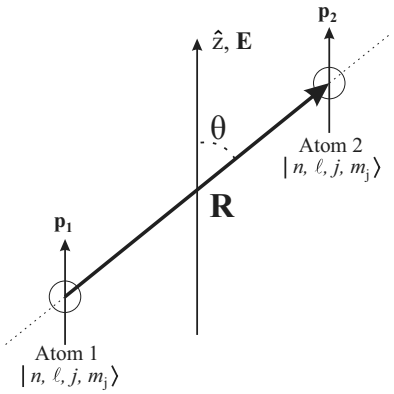

FIG. 2. Two interacting Rydberg atoms separated by a vector **R** which defines an angle θ with the quantization ($\hat{\mathbf{z}}$) axis. In cases where an electric field **E** is applied, the field is parallel to the quantization axis.

$$V_{dd}=\frac{p_{1+}p_{2-}+p_{1-}p_{2+}+p_{1z}p_{2z}(1-3\cos^2\theta)}{R^3}-\frac{\frac{3}{2}\sin^2\theta(p_{1+}p_{2+}+p_{1+}p_{2-}+p_{1-}p_{2+}+p_{1-}p_{2-})}{R^3}-\frac{\frac{3}{\sqrt{2}}\sin\theta\cos\theta(p_{1+}p_{2z}+p_{1-}p_{2z}+p_{1z}p_{2+}+p_{1z}p_{2-})}{R^3}, \tag{2}$$

where the first subscript of the p components identifies the atom number, $p_{\pm}=\frac{1}{\sqrt{2}}(x\pm iy)$, and $p_z=z$ (in atomic units). The matrix elements of V_{dd} are independent of the azimuthal angle of **R**. From this expression, we see that calculating two-particle matrix elements of V_{dd} involves evaluating the single-particle matrix elements $\langle n',\ell',j',m_j'|p_{\alpha,\beta}|n,\ell,j,m_j\rangle$ where α is the particle number and $\beta\in\{+,-,z\}$.

In the following, we explain the essential details of the numerical method used to obtain the single-particle radial wave functions, $\psi(r)$, required to calculate the matrix elements $\langle n',\ell',j',m_j'|p_{\alpha,\beta}|n,\ell,j,m_j\rangle$. The radial wave functions are integrated using an algorithm that continuously adjusts the step size such that it is smaller than, but close to, $2\pi/\tilde{v}$ divided by a constant, f, where $\tilde{v}=\sqrt{|2E+2/r-l(l+1)/r^2|}$ (in atomic units; E is the single-particle level energy). In the classically allowed region, the step size approximately equals the de Broglie wavelength divided by f. To ensure reliable integration through the classical turning points, where the local wavelength diverges, the step size is limited to a maximal value of $d_{\max}$. For the data presented in this paper, the step size parameters have been set to $f=200$ and $d_{\max}=1$. Since the local wavelength of the Rydberg-electron wave function is very large at locations far away from the core, the step-size adjustment considerably speeds up the integration. The accuracy is consistent because the number of points per wavelength at which the wave function is determined is approximately fixed. The wave

functions are integrated inward. Assuming that the wave function has known values ψ_0 and ψ_p at locations r_0 and r_p, respectively ($r_0 < r_p$), a location r_m is determined using the above stepwidth rules [$r_m < r_0$ and $r_0 - r_m \leq \min(d_{\max}, 2\pi/\{\bar{v}(r_0)f\})$]. To determine the wave function ψ_m at location r_m, we use

$$h = (r_p - r_0)(r_0 - r_m)(r_p - r_m),$$

$$f_p = 2(r_0 - r_m)/h,$$

$$f_m = 2(r_p - r_0)/h,$$

$$\psi_m = \{[-p^2(r_0) + f_p + f_m]\psi_0 - f_p\psi_p\}/f_m,$$

where $p^2(r) = 2E + 2/r - l(l+1)/r^2$. This method allows for continuous changes of the step size $r_0 - r_m$. To estimate the effect of numerical errors in the wave-function calculations on the van der Waals level shifts, we have performed testcalculations with finer step sizes (parameters $f = 400$ and $d_{\max} = 0.3$). Based on the results, the numerical errors of the van der Waals level shifts presented here are estimated at about 1% or less.

To calculate van der Waals energy level shifts due to V_{dd} in zero external electric field, we sum the level shifts due to many perturbing channels in second-order perturbation theory using the calculated matrix elements of V_{dd}. Explicitly, the van der Waals shift of the two-particle state $2 \times |n, \ell, j, m_j\rangle$ is given by the sum

$$\Delta W^{(2)} = -\sum_{\substack{n',\ell',j',m_j', \\ n'',\ell'',j'',m_j''}} \frac{|\langle n'',\ell'',j'',m_j''| \otimes \langle n',\ell',j',m_j'|V_{dd}|n,\ell,j,m_j\rangle \otimes |n,\ell,j,m_j\rangle|^2}{\Delta}, \tag{3}$$

where $\Delta \equiv W_{|n'',\ell'',j'',m_j''\rangle} + W_{|n',\ell',j',m_j'\rangle} - 2W_{|n,\ell,j,m_j\rangle}$ is the infinite-separation energy defect. To reduce the amount of data in the calculation, we only include two-particle couplings with $|\langle \cdots | V_{dd} | \cdots \rangle| > 10^{-4} n^{*4}/R^3$, where $n^* = n - \delta_\ell$ is the effective principal quantum number. It is noted that all elements of V_{dd} are calculated before the small ones are discarded. Furthermore, in the sum in Eq. (3) we only include terms with $|\Delta| < 100$ GHz. We have confirmed in test calculations with unlimited $|\Delta|$, which have included all couplings as small as $|\langle \cdots | V_{dd} | \cdots \rangle| > 10^{-6} n^{*4}/R^3$, that the described limitation of the sum in Eq. (3) does not change the calculated van der Waals shifts by more than about 1%. By restricting the sum in the described way, we find that typically of the order of hundreds of two-particle states $|n',\ell',j',m_j'\rangle \otimes |n'',\ell'',j'',m_j''\rangle$ still contribute, although the dominant contributions usually come from only 5 to 10 two-particle states, with one or two of those often accounting for 70%–90% of the level shift.

In our calculations, we have included single-particle basis states with principal quantum numbers over a restricted n-range and have verified that the inclusion of more bound states does not noticeably change the results. We have not included continuum states in our calculation. Continuum states are important in calculations of van der Waals shifts of atomic ground states or low-lying states, where in the sum in Eq. (3) there are no near-resonant terms with very small Δ. For instance, for basic estimates of ground-state level shifts, one may approximate all energy denominators by the ionization energy and use a closure relation to compute the sum in Eq. (3) [30]. The closure relation incorporates all continuum states. In contrast, for Rydberg-atom pairs the energy denominators in Eq. (3) vary from tens of MHz for the near-resonant two-particle states to about 10^{15} Hz for two-particle states near the ground state, leading to an enormous variation in the significance of terms. Typically, there are several near-resonant terms, and it is found that those dominate the van der Waals shifts of Rydberg atoms. We believe that due to this resonant behavior the introduction of continuum states will not make a significant difference.

In Sec. III we calculate the energy shifts, $\Delta W^{(2)}$, as a function of the quantum numbers and the angle θ of the interacting Rydberg atoms (see Fig. 2) in the absence of an applied external electric field.

In cases where an external electric field is applied, the field-free eigenstates, $|n,\ell,j,m_j\rangle$, are no longer eigenstates of the single-atom Hamiltonian. Therefore, to proceed with a perturbative calculation of the binary interaction energies, we first calculate the single-atom eigenstates of the Hamiltonian $H = H_{\text{at}} + Ez$, where H_{at} is the field-free, single-atom Hamiltonian and $\mathbf{E} = E\hat{\mathbf{z}}$ is the applied electric field. We label the single-atom eigenstates as $|\lambda, m_j\rangle$, where λ is an index which uniquely identifies each Stark state of a given m_j.

If two Rydberg atoms interact in the presence of an applied electric field, both first- and second-order interaction energies occur. Since the Stark eigenstates are not states of definite parity, the diagonal single-atom matrix elements $\langle \lambda, m_j | p_{\alpha,z} | \lambda, m_j \rangle$ of the dipole operator are nonzero. This leads to a first-order dipole-dipole interaction energy of the type

$$\Delta W^{(1)} = \langle \lambda, m_j | \otimes \langle \lambda, m_j | V_{dd} | \lambda, m_j \rangle \otimes | \lambda, m_j \rangle. \tag{4}$$

If the Stark eigenstates have large permanent electric dipole moments, $\langle \lambda, m_j | p_{\alpha,z} | \lambda, m_j \rangle$, the level shift in Eq. (4) dominates, as discussed in Sec. V A.

In another scheme, the electric field may be used to tune two distinct two-particle states $|\lambda, m_j\rangle \otimes |\lambda, m_j\rangle$ and

$|\lambda',m_j'\rangle \otimes |\lambda'',m_j''\rangle$ into exact resonance ($\Delta = W_{|\lambda',m_j'\rangle} + W_{|\lambda'',m_j''\rangle} - 2W_{|\lambda,m_j\rangle} = 0$). These resonances are referred to as Förster resonances. In the case of a Förster resonance, diagonalization of the two-particle Hamiltonian within the subspace of degenerate two-particle states leads to mixed eigenstates with first-order dipole-dipole energy level shifts of

$$\Delta W^{(1)} = \pm \langle \lambda',m_j'| \otimes \langle \lambda'',m_j''|V_{dd}|\lambda,m_j\rangle \otimes |\lambda,m_j\rangle, \quad (5)$$

which can dominate all other level shifts, as discussed in detail in Sec. V B.

In cases where the Stark eigenstates have negligible permanent dipole moments and there are no electric-field-induced Förster resonances, there still exists a second-order van der Waals interaction of the type

$$\Delta W^{(2)} = -\sum_{\substack{\lambda',m_j',\lambda'',m_j'' \\ \Delta \neq 0}} \frac{|\langle \lambda'',m_j''| \otimes \langle \lambda',m_j'|V_{dd}|\lambda,m_j\rangle \otimes |\lambda,m_j\rangle|^2}{\Delta} \quad (6)$$

which may lead to significant level shifts. As an example, in Sec. V C we examine the van der Waals level shifts of a specific two-particle state as a function of θ and E.

III. LEVEL SHIFTS IN ZERO ELECTRIC FIELD

A. Rb $nD_{5/2}$ Rydberg states

In many experiments, Rydberg excitations are created via a two-step process from a ground S state to $S_{1/2}$, $D_{3/2}$, and $D_{5/2}$ Rydberg states, through an intermediate P state. Since the transitions into $D_{5/2}$ states have the highest oscillator strength, these states are often studied experimentally [14,20,24]. Thus, we first investigate the binary interaction-induced energy level shifts for $nD_{5/2}$ Rydberg states of Rb in zero applied electric field.

In Fig. 3, we present scaled binary energy level shifts of $2\times|nD_{5/2},m_j\rangle$ states as a function of n at $\theta=0$ (a) and as a function of θ at $n=60$ (b). The scaled level shifts are defined by

$$\Delta\tilde{W}^{(2)}(n,\ell,j,m_j,\theta) \equiv \Delta W^{(2)}(n,\ell,j,m_j,R,\theta)(R^6/n^{*11}), \quad (7)$$

with $\Delta W^{(2)}(n,\ell,j,m_j,R,\theta)$ given in Eq. (3). Due to the scaling, the scaled shift $\Delta\tilde{W}^{(2)}$ does not depend on R.

In Fig. 3(a), we can distinguish between regions of qualitatively different behavior. In the ranges $n \gtrsim 50$ and $n \lesssim 35$, the scaled energy shift is roughly a constant function of n for any given m_j, while in the range $35 \lesssim n \lesssim 50$ it is characterized by a prominent dispersive feature. These differences can be attributed to the number of relevant channels in Eq. (3) and their dependence on n.

In the ranges $n \gtrsim 50$ and $n \lesssim 35$, the channel,

$$2 \times nD_{5/2} \rightarrow (n-1)F_{7/2} + (n+1)P_{3/2}, \quad (8)$$

dominates all other channels in the sum in Eq. (3) and accounts for roughly 70%–80% of the total energy shift. The product-state sum indices m_j' and m_j'' of Eq. (3) are omitted in the channel notation used in Eq. (8). In many cases the channel in Eq. (8) has multiple subchannels that correspond to different dipole-allowed combinations of m_j' and m_j''. The allowed subchannels have fairly large coupling strengths $|\langle\cdots|V_{\rm dd}|\cdots\rangle| \sim 1 n^{*4}/R^3$, where the numerical prefactor "1" depends somewhat on θ and on the m_j values. However, the allowed subchannels also have large energy denominators $\left[\Delta \approx 1\ \text{GHz} \times \left(\frac{58}{n^*}\right)^3\right]$, which limit the magnitude of the resultant second-order shift. Because of the n^{*4}/R^3 scaling of the couplings and the $1/n^{*3}$ scaling of Δ, the contribution to the second-order shift due to this strong, highly detuned channel scales as n^{*11}/R^6. Since in the ranges $n \gtrsim 50$ and $n \lesssim 35$ this contribution dominates, the scaled shifts $\Delta\tilde{W}^{(2)}$ are approximately constant, as observed in Fig. 3.

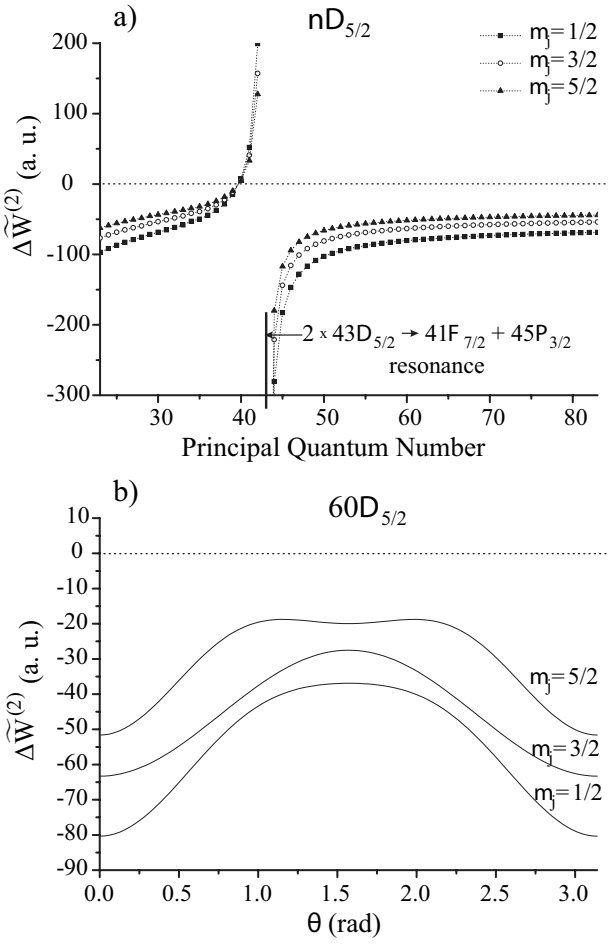

FIG. 3. (a) Scaled energy level shifts, $\Delta\tilde{W}^{(2)}$, as defined in Eq. (7), of $2\times|nD_{5/2},m_j\rangle$ states as a function of n for different m_j quantum numbers and $\theta=0$. (b) $\Delta\tilde{W}^{(2)}$ of $2\times|60D_{5/2},m_j\rangle$ states as a function of θ for different m_j quantum numbers.

In the range $35 \lesssim n \lesssim 50$, a different, nearly resonant channel significantly contributes to the perturbative sum and interrupts the n^{*11}/R^6 scaling of the energy shifts. This channel,

$$2 \times nD_{5/2} \rightarrow (n-2)F_{7/2} + (n+2)P_{3/2}, \quad (9)$$

has a coupling strength $|\langle\cdots|V_{\rm dd}|\cdots\rangle| \sim 0.36 n^{*4}/R^3$ in the vicinity of $n=43$ and a small, nearly resonant energy denomi-

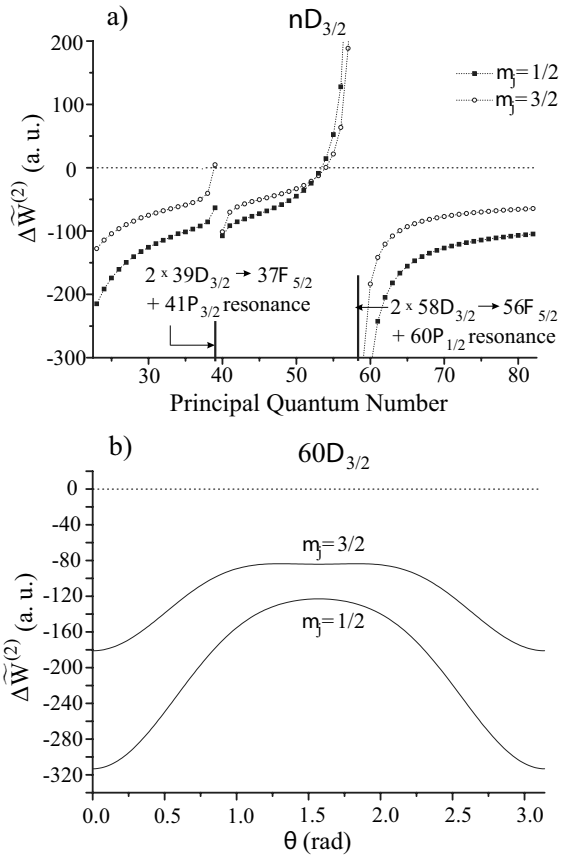

FIG. 4. (a) Scaled energy level shifts, $\Delta\tilde{W}^{(2)}$, of $2\times|nD_{3/2},m_j\rangle$ states as a function of n for different m_j quantum numbers and $\theta=0$. (b) $\Delta\tilde{W}^{(2)}$ of $2\times|60D_{3/2},m_j\rangle$ states as a function of θ for different m_j quantum numbers.

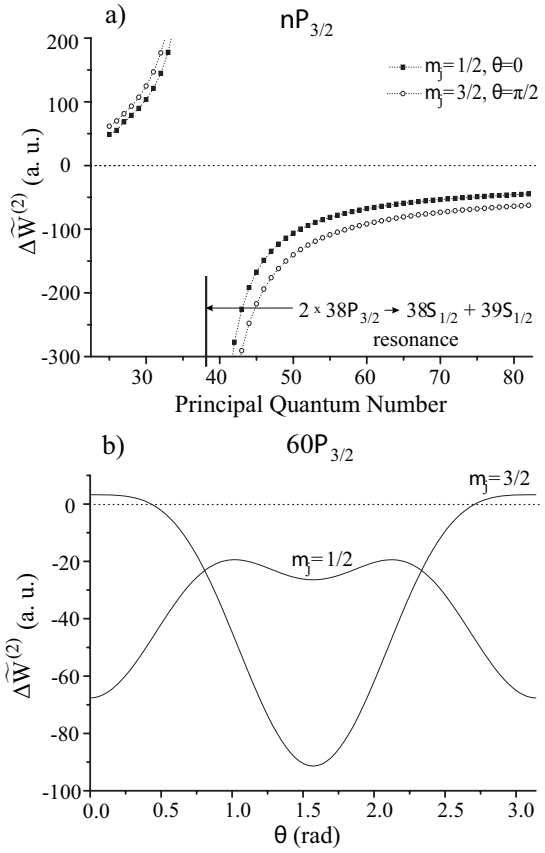

FIG. 5. (a) Scaled energy level shifts, $\Delta\tilde{W}^{(2)}$, of $2\times|nP_{3/2},m_j\rangle$ states as a function of n for different m_j quantum numbers and different θ. (b) $\Delta\tilde{W}^{(2)}$ of $2\times|60P_{3/2},m_j\rangle$ states as a function of θ for different m_j quantum numbers.

nator of $\Delta\approx 71(n^*-41.6)$ MHz, i.e., the energy denominator undergoes a zero crossing between $n=42$ and 43. In the vicinity of $n=43$, the scaled level shift of the state $2\times|nD_{5/2},m_j=5/2\rangle$ due to the channels in Eqs. (8) and (9) approximately follows, for $\theta=0$,

$$\Delta\tilde{W}^{(2)}\approx-\left(35+\frac{160}{(n^*-41.6)}\right), \tag{10}$$

in the same units as in Fig. 3. In the range $40\leqslant n\leqslant 47$, the level shift due to the near-resonant channel [Eq. (9) and second term in Eq. (10)] is greater than that due to the off-resonant channel [Eq. (8) and first term in Eq. (10)]. Since these two terms have different n dependencies, the total shift does not follow a simple scaling law in this n range.

The scaled level shifts in Fig. 3 are obtained perturbatively, and therefore care must be taken when interpreting and using them. For any given n and R, one may determine the absolute van der Waals level shift (in atomic units) from Fig. 3 by multiplying the scaled shift with n^{*11}/R^6. However, the result is only valid if, for the significant terms in the sum in Eq. (3), the coupling strengths $|\langle\cdots|V_{dd}|\cdots\rangle|$ are smaller than their energy denominators Δ. Generally, for each two-particle Rydberg state $2\times|n,\ell,j,m_j\rangle$ a critical radius R_c exists such that the perturbative method is valid for $R>R_c$. Analogous considerations apply to Figs. 4–6.

The n dependence of the energy shifts depicted in Fig. 3(a) offers possible methods to control the Rydberg blockade. For excitation into $2\times|nD_{5/2},m_j=5/2\rangle$ states by a laser of reasonably small bandwidth (often a few MHz) and typical Rydberg atom separations (several μm in most atom traps), one would expect the blockade to begin to manifest itself at $n\sim 50$, where the energy shift roughly equals the laser linewidth. Since for $n\gtrsim 50$ the shifts grow smoothly as n^{*11}, the blockade should rapidly become more effective as n is increased. In the range $n\lesssim 50$, the shifts will generally be too small to cause an observable blockade effect, except in the immediate vicinity of $n=43$, where the resonance in Eq. (9) causes appreciable energy level shifts.

The scaled level shifts of the two-particle states $2\times|60D_{5/2},m_j\rangle$ as a function of θ are shown in Fig. 3(b). Analogous curves for different $2\times|nD_{5/2},m_j\rangle$ states can approximately be obtained by multiplying the curves shown in Fig. 3(b) by the ratios

$$\frac{\Delta\tilde{W}^{(2)}(n,l=2,j=5/2,m_j,\theta=0)}{\Delta\tilde{W}^{(2)}(n=60,l=2,j=5/2,m_j,\theta=0)},$$

which follow from the data shown in Fig. 3(a). The similarity among the curves $\Delta\tilde{W}^{(2)}(n,l=2,j=5/2,m_j,\theta)$ vs θ for dif-

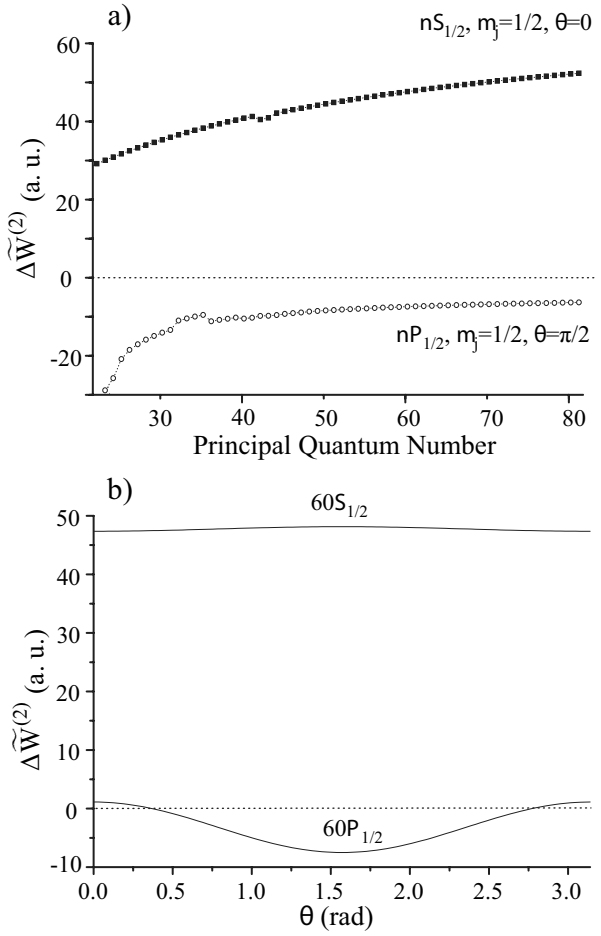

FIG. 6. (a) Scaled energy level shifts, $\Delta\tilde{W}^{(2)}$, of $2\times|nP_{1/2},m_j\rangle$ and $2\times|nS_{1/2},m_j\rangle$ states as a function of n for different θ. (b) $\Delta\tilde{W}^{(2)}$ of $2\times|60P_{1/2},m_j\rangle$ and $2\times|60S_{1/2},m_j\rangle$ states as a function of θ.

ferent n relies on the fact that the dominant channels, Eqs. (8) and (9), have the same angular-momentum quantum numbers.

B. Other low-angular-momentum Rb Rydberg states

In this section we examine the scaled energy level shifts, $\Delta\tilde{W}^{(2)}$, as a function of n and θ for excitation into $nD_{3/2}$, $nP_{3/2}$, $nP_{1/2}$, and $nS_{1/2}$ Rydberg states. In parts (a) of Figs. 4–6, we plot the scaled level shifts as a function of n for specific θ values which yield large level shifts ($\theta=0$ or $\pi/2$). In parts (b) of Figs. 4–6, we plot the scaled level shifts as a function of θ at fixed $n=60$. In the following, we discuss some qualitative features of these plots.

The scaled energy level shifts of the states $2\times|nD_{3/2},m_j\rangle$, shown in Fig. 4(a), exhibit a behavior similar to that of the states $2\times|nD_{5/2},m_j\rangle$, except that two interaction channels, $2\times nD_{3/2}\rightarrow(n-2)F_{5/2}+(n+2)P_{3/2}$ and $2\times nD_{3/2}\rightarrow(n-2)F_{5/2}+(n+2)P_{1/2}$, become nearly resonant at $n=39$ and $n=58$, respectively. The resonances manifest themselves as dispersive-shaped features. The resonance centered at $n=39$ is weaker than the one at $n=58$ due to a smaller coupling strength, $|\langle\cdots|V_{dd}|\cdots\rangle|$. Away from these two resonances, the scaled shift varies little with n because an off-resonant channel with large coupling strength, $2\times nD_{3/2}\rightarrow(n-1)F_{5/2}+(n+1)P_{1/2}$, is responsible for the majority ($\gtrsim 60\%$) of the level shift. The dependence of the scaled level shifts of $2\times|nD_{3/2},m_j\rangle$ on θ, shown in Fig. 4(b), resembles that of $2\times|nD_{5/2},m_j\rangle$, shown in Fig. 3(b). In both cases, the level shifts are always negative and only moderately sensitive to θ. The considerable difference in the respective magnitudes of the level shifts is due to the fact that the case $n=60$ happens to be quite close to a resonance in Fig. 4(a) but not in Fig. 3(a).

Figure 5(a) shows $\Delta\tilde{W}^{(2)}$ as a function of n for excitation into $2\times|nP_{3/2},m_j\rangle$ states, which exhibits a dispersive-shaped feature centered at $n=38$ that has about the same width as that in Fig. 3(a). The energy detuning, Δ, of the responsible near-resonant channel, $2\times nP_{3/2}\rightarrow nS_{1/2}+(n+1)S_{1/2}$, varies about as rapidly with n as that of the channel in Eq. (9), while the coupling strength, $|\langle\cdots|V_{dd}|\cdots\rangle|$, is a factor of 2 larger. The channel $2\times nP_{3/2}\rightarrow nS_{1/2}+(n+1)S_{1/2}$ accounts for greater than 90% of the level shifts of $2\times|nP_{3/2},m_j\rangle$ states over the whole n-range displayed in Fig. 5(a), and no other off-resonant channel contributes significantly. Far away from resonance, the energy detuning of this channel tends to scale as n^{*-3}, leading to scaled energy shifts that are approximately constant as a function of n. As seen in Fig. 5(b), the θ dependence of the shifts for the $2\times|60P_{3/2},m_j=1/2\rangle$ states resembles that for the $60D_{5/2}$ and $60D_{3/2}$ states. The shifts for the $2\times|60P_{3/2},m_j=3/2\rangle$ states, however, have a strong variation that appears to be $\propto\sin^2\theta$. This is because for $m_j=3/2$ the product states of the transition $2\times nP_{3/2}\rightarrow nS_{1/2}+(n+1)S_{1/2}$ must have $m_j'=m_j''=1/2$, leaving only the $p_{1-}p_{2-}\sin^2\theta$ term in Eq. (2). Other weakly contributing channels cause slight deviations from a pure $\sin^2\theta$ dependence and cause the level shifts to vanish and to change signs at $\theta\approx 0.43$ and 2.71 rad.

The scaled level shifts as a function of n for excitation into $2\times|nP_{1/2},m_j=1/2\rangle$ states, shown in the lower curve of Fig. 6(a), are relatively small and negative. In the displayed n range, the level shifts vary only moderately with n. The channel $2\times nP_{1/2}\rightarrow nS_{1/2}+(n+1)S_{1/2}$ is responsible for $\geqslant 90\%$ of the shifts. Neither this channel nor any other significant channel becomes resonant at any n in the displayed range. The θ dependence of the scaled level shifts of the state $2\times|60P_{1/2},m_j=1/2\rangle$, shown in Fig. 6(b), resembles that of the state $2\times|60P_{3/2},m_j=3/2\rangle$ (but the shifts of $2\times|60P_{1/2},m_j=1/2\rangle$ are about 10 times less than those of $2\times|60P_{3/2},m_j=3/2\rangle$). This indicates that for the shifts of $2\times|nP_{1/2},m_j=1/2\rangle$ the term $p_{1-}p_{2-}\sin^2\theta$ in Eq. (2) also is dominant; we have confirmed that this is the case by inspecting the relative magnitudes of the dipole-allowed terms.

The scaled level shifts of the states $2\times|nS_{1/2},m_j=1/2\rangle$, shown in Figs. 6(a) and 6(b), are qualitatively different from all other cases discussed in this paper in that they are large and positive for all n and θ. Four channels of the type $2\times nS_{1/2}\rightarrow nP_{j'}+(n-1)P_{j''}$ account for most of the level shift in the displayed region, where $j',j''=1/2$ or $3/2$. None of the channels becomes resonant at any n in the displayed range. The level shifts of the states $2\times|nS_{1/2},m_j=1/2\rangle$ are almost entirely independent of θ, reflecting the spherical

symmetry of *s*-state wave functions. (The shifts are not entirely spherically symmetric because of spin orientation effects and fine-structure coupling.)

In all cases discussed so far, the detailed values of the infinite-separation energy defect, Δ, depend sensitively on the accuracy and precision of quantum defects used in the calculations. We have used quantum defects for Rb from Ref. [34]. Comparing the results to values obtained with alternative sets of quantum defects from other sources, i.e., Ref. [35] and Ref. [36], we have seen that typically the energy detunings, Δ, vary by amounts of order tens of MHz. Variations of that size significantly affect the energy shifts only very close to the resonances in Figs. 3–5. These variations can change the n values where the resonances occur by ± 1.

C. Applications of the level-shift calculations

Figures 3–6 enable one to choose Rydberg states with properties that are appropriate for specific applications. For example, in quantum-information-processing applications, states with level shifts that are large and relatively insensitive to variations in θ and magnetic quantum numbers are desirable. If Rydberg states with these interaction properties are used, experimental variations in angle and polarization will not translate into excessive gate inefficiencies. Inspecting Figs. 3–6 it is seen that large shifts may be obtained by choosing a principal quantum number near an interaction resonance, e.g., near $n=58$ for excitation into $D_{3/2}$ states. Another way to achieve large shifts is to exploit the generic van der Waals scaling (absolute shift $\propto n^{*11}$ for sufficiently large atom-atom separation), which in almost all cases studied leads to large shifts for $n \gtrsim 70$ (except for the $P_{1/2}$ states). The requirement of low sensitivity of the level shifts to variations in θ and magnetic quantum numbers excludes $P_{3/2}$ and $P_{1/2}$ states. Rydberg atoms in $nS_{1/2}$ states appear to be particularly attractive candidates, because their energy shifts are large, near-isotropic, and positive, leading to mutual repulsion between atoms and therefore inhibition of ionizing interactions triggered by attractive forces between atoms [5].

Figures 3–6 can also be used to select Rb Rydberg states in applications of dense Rydberg-atom gases and cold plasmas. In cases where state-changing and ionizing collisions between atoms are not desired, one looks for positive energy level shifts with weak dependence on magnetic quantum numbers and θ. These properties lead to repulsive forces between atoms that inhibit close, inelastic collisions. Among the cases studied, all $nS_{1/2}$ states and nD states in limited, small ranges of n ($n=41-43$ for $D_{5/2}$ and $n=55-57$ for $D_{3/2}$) meet these requirements. Alternatively, one may accelerate the onset of collision-induced effects by choosing states with negative, large, and resonantly enhanced shifts, e.g., $nD_{5/2}$ with $n \approx 44$, $nD_{3/2}$ with $n \approx 59$, or $nP_{3/2}$ with $n \approx 40$. A dense cloud of Rydberg atoms initially prepared in one of these states will exhibit a high initial rate of atom-atom collisions triggered by attractive forces between the atoms, leading to rapid ionization and accelerated transition of the cloud into a cold plasma.

One may anticipate applications in which the magnitude and the polar angle, θ, of the relative vector, $\mathbf{R}$, between the interacting Rydberg atoms can be controlled using optical lattices or other types of miniature atom traps. In such cases, one may choose states whose level shifts depend strongly on θ, such as the states $2 \times |nP_{3/2}, m_j = 3/2\rangle$. In this scenario, the interaction strength between the atoms can be controlled by controlling θ.

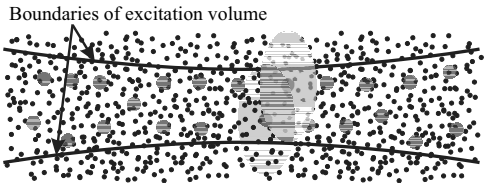

FIG. 7. Graphical representation of a Rydberg-excitation blockade inside an extended atomic ensemble. Within the boundaries of the excitation volume (lines), Rydberg excitations created in a cloud of ground state atoms (dots) are localized and detected at certain atoms (dark gray spheres) using a quantum measurement process. Due to the Rydberg blockade, each detected Rydberg atom defines a volume V_{se} (light gray regions) in which no other Rydberg atoms can be detected.

IV. RELEVANCE TO A RYDBERG-BLOCKADE EXPERIMENT

Recently, the effectiveness of the Rydberg blockade for ^{85}Rb $nD_{5/2}$ atoms in an electric-field-free environment has been measured as a function of principal quantum number using the counting statistics of detected Rydberg atoms [14]. In this section, we use the results obtained in Sec. III A to explain important trends observed in this experiment. Due to the finite range of Rydberg-Rydberg interactions, if an atomic ensemble is uniformly excited into Rydberg states and a Rydberg blockade is effective, the excitation volume will break up into regions within which, ideally, only a single Rydberg excitation can be present. These regions have a volume V_{se} that corresponds to the volume over which the autocorrelation function of Rydberg excitations in the many-body system is approximately zero [16]. Exploiting the rules of quantum measurement, this autocorrelation function can, in principle, be profiled in an experiment in which the delocalized Rydberg excitations present in the sample are projected onto individual atoms and detected with high spatial resolution. This measurement can be accomplished by electric-field ionization of the Rydberg atoms and detection of the liberated electrons with a position-sensitive microchannel plate detector. In the measurement result, each detected, localized Rydberg excitation is surrounded by a "bubble" of volume V_{se} within which no other Rydberg excitation can be detected. In Fig. 7, two single-excitation volumes are indicated as gray "bubbles." Qualitatively, the radius of these regions is given by the distance R_{se} at which the interaction potential of interacting Rydberg atoms equals h times the laser linewidth. If the volume V_{se} is large enough to contain a significant number of ground-state atoms, then the number of Rydberg excitations in the system is approximately constant and given by the excitation volume divided by $V_{se}/8$. There, the factor $1/8$ is due to the fact that, in a three-dimensional configuration, of order eight single-excitation regions may overlap each other. If the Rydberg

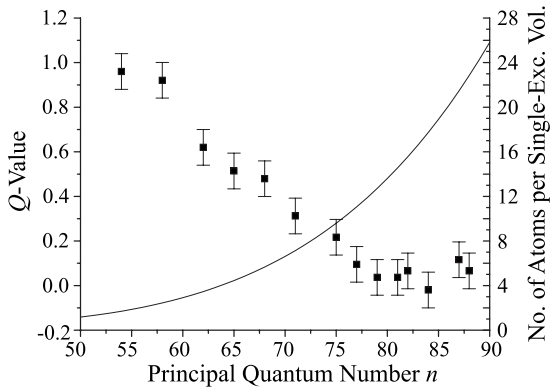

FIG. 8. The symbols depict Q-values measured as a function of principal quantum number n (Ref. [14], left-hand axis). The average number of detected Rydberg atoms was kept constant at about 30. The line shows the calculated number of atoms in the single-excitation volume, V_{se}, using the interaction energies of Fig. 3 (right axis).

blockade is effective, fluctuations in the number of ground state atoms do not translate into fluctuations in the number of Rydberg excitations. Thus, sub-Poissonian distributions of the Rydberg-atom number are an expected signature of the blockade effect [14,16,17].

The Mandel Q-parameter, used to characterize the width of statistical distributions, is defined as the variance in the distribution divided by the mean number of counts, minus one, $Q \equiv \frac{\langle N_e^2\rangle - \langle N_e\rangle^2}{\langle N_e\rangle} - 1$ [31]. For a given distribution of Rydberg counts, the closer Q is to -1, the more sub-Poissonian the distribution and the more effective the blockade. For uncorrelated, unblockaded excitation in real systems, one would expect to obtain Poissonian counting statistics ($Q \sim 0$). The Q-value provides a quantitative measure for blockade effectiveness that is particularly well suited for small atomic samples with few Rydberg excitations. The Q value can be used to quantify the effect of parameters such as atom density, laser detuning, and Rydberg-state quantum numbers on the blockade. In Fig. 8, the data points (referenced to the left y axis) represent Q values measured for excitation into $nD_{5/2}$ states as a function of principal quantum number.

The calculations of the energy level shifts presented in this paper provide considerable insight into the experimental data presented in Fig. 8. First, since the experiments were performed on ensembles of randomly placed atoms, they did not show how the energy shifts of $D_{5/2}$ states depend on the angle θ. The theoretical results presented in Fig. 3(b) reveal that the scaled shifts are large in magnitude for all θ, never change sign, and do not vary by more than a factor of 2 as a function of θ. The robustness of the level shifts against experimental θ variations is consistent with the observation of a blockade effect in Fig. 8.

Second, the results of Sec. III A also explain why the Q-values exhibit a smooth transition from $Q \sim 1$ at low n to $Q \sim 0$ at high n. Any strong resonance of the type apparent in Figs. 3–5 would lead to an enhancement of the energy level shifts and, therefore, to a dip in the Q-value centered at the principal quantum number at which the resonance occurs. The scaled van der Waals level shifts in Fig. 3(a) reveal that over the range studied experimentally, $54 \leqslant n \leqslant 88$ [14], there is no resonant channel for $nD_{5/2}$ states, and consequently the energy shifts scale smoothly with n as n^{*11}. This translates into a smooth increase of the blockade effectiveness and a smooth decrease of the Q-value with increasing n.

This smooth scaling is further illustrated by examining how many atoms are in the single-excitation volume, V_{se}, as a function of n. The volume V_{se} can be estimated by

$$V_{se}(n) = 2\pi \int_0^{\pi} \sin\theta d\theta \int_0^{R_{se}(n,\theta)} r^2 dr, \tag{11}$$

where $R_{se}(n,\theta)$ is the radial coordinate of the surface at a given n and polar angle θ at which the energy level shift equals the laser linewidth (5 MHz in the experiment). We determine $R_{se}(n,\theta)$ by solving

$$\Delta W^{(2)}(n,R,\theta) = h \times 5 \text{ MHz}$$

for R, where $\Delta W^{(2)}$ is given in Eq. (3). Due to the anisotropy of the Rydberg-Rydberg interaction, the single-excitation volume will, in general, not be spherical, as indicated by the elliptical shapes in Fig. 8. To model the experiment in Ref. [14], in our calculation we use $l=2$, $j=5/2$, and $m_j=5/2$ in the expression for $\Delta W^{(2)}$. To estimate the number of all atoms N_{se} in V_{se} as a function of n, we multiply the values of $V_{se}(n)$ obtained from Eq. (11) by the ground-state atom density (5×10^9 cm^{-3} in Ref. [14]). Both ground state and Rydberg atoms are included in N_{se}, and the number of atoms in the sample per Rydberg excitation created is approximately given by $N_{se}/8$ (the factor $1/8$ is due to the fact that of order eight single-excitation regions may overlap each other). The results for N_{se} are shown as the solid line in Fig. 8 (referenced to the right-hand y axis). At $n \approx 55$, where the Rydberg-atom counting distribution has a $Q \sim 1$, $N_{se} \sim 2$. This value is too low to ensure the creation of one Rydberg excitation in each single-excitation region. The resultant uncertainty in the overall number of Rydberg excitations in the whole atomic sample, together with technical noise, results in Rydberg-atom counting distributions with $Q \sim 1$, as observed experimentally for $n \lesssim 55$. For $n \gtrsim 75$, where the Q values saturate at about 0, N_{se} varies from approximately 10 to 26. This range is sufficiently high to ensure the creation of a Rydberg excitation in each single-excitation region. It should be noted that our estimates of N_{se} depend sensitively on the assumed ground-state atom density (5×10^9 cm^{-3}) and the assumed laser linewidth (5 MHz) in the experiment. Since the assumed values represent conservative estimates, we believe that the actual values of N_{se} are considerably larger than the ones shown in Fig. 8.

In the following we comment on the values of the measured Mandel Q parameter displayed in 8. At low n, where the blockade is not expected to be effective, we observe $Q \sim 1$, indicative of super-Poissonian distributions. At high n, where the blockade is expected to be effective, we observe $Q \sim 0$, indicative of narrower but not quite sub-Poissonian distributions [37]. Evidently, at low n technical noise (e.g., super-Poissonian shot-to-shot fluctuations of the ground-state

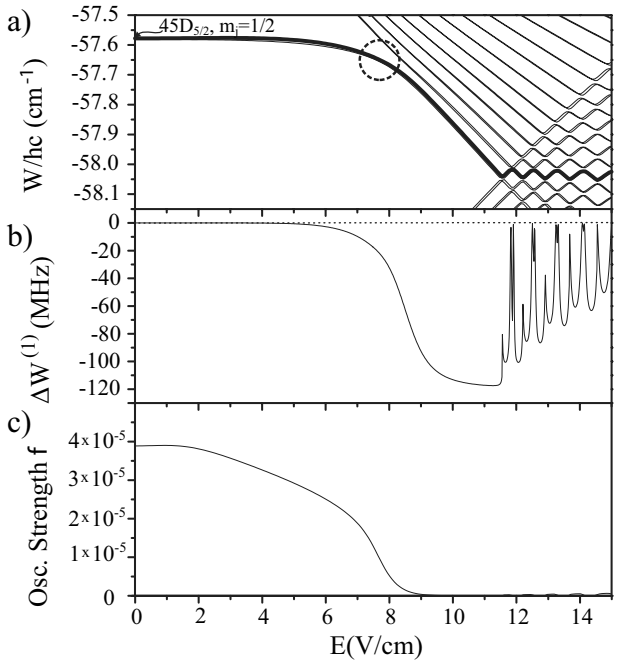

FIG. 9. (a) Stark map of the $m_j=1/2$-manifold of Rb in the vicinity of the $45D$ energy level vs electric field E. The energy W is relative to the ionization potential. Levels with large permanent electric dipole moment and large oscillator strength from the low-lying P states are found within the dashed circle. The bold level identifies the state that converges to $|45D_{5/2},m_j=1/2\rangle$ at $E=0$. (b) Level shift $\Delta W^{(1)}$ due to permanent-electric-dipole interaction of the two-atom state that converges to $2\times|45D_{5/2},m_j=1/2\rangle$ at zero field vs E for $R=5$ μm and $\theta=0$. (c) Oscillator strength for π excitation from the $|5P_{3/2},m_j=1/2\rangle$ state into the state that converges to $|45D_{5/2},m_j=1/2\rangle$ at $E=0$.

atom number and variations in the single-atom excitation efficiency) causes the statistics to be super-Poissonian ($Q\sim1$). At large n, the Rydberg excitation number distributions are significantly narrowed by the blockade effect, causing the Q value to decrease from 1 to about 0. In the absence of technical noise, one would expect $Q\sim0$ at low n and substantially negative at high n [16,17]. The trends in the function Q vs n are, however, unaffected by technical noise. Regardless of the level of technical noise, the blockade causes a significant reduction in the value of Q.

V. LEVEL SHIFTS IN EXTERNAL ELECTRIC FIELDS

In Sec. IV we have seen that the strength of binary interactions between Rydberg atoms can be varied using static parameters of the system, such as the quantum numbers of the Rydberg level excited. Applications of the Rydberg-excitation blockade, e.g., in quantum information processing, may benefit from dynamic control methods that enable reproducible, rapid, and real-time variations of the interaction strength. An external electric field applied to the atoms is a readily accessible dynamic control parameter. In this section, we discuss level shifts due to binary Rydberg-Rydberg interactions in external electric fields. In one scheme, discussed in Sec. V A, a fairly strong electric field is applied so that the Rydberg states have large permanent dipole moments, leading to large first-order energy shifts that can be calculated according to Eq. (4). In an alternative interaction scheme discussed in Sec. V B, a weak electric field is applied in order to tune a well-defined interaction channel of the type $|\lambda,m_j\rangle\otimes|\lambda,m_j\rangle\rightarrow|\lambda',m_j'\rangle\otimes|\lambda'',m_j''\rangle$ into resonance. In the case of exact resonance, the resultant shifts are first order and can be calculated using Eq. (5). In cases where an electric field is applied but there is no resonant, first-order shift, there are usually still significant second-order, van der Waals shifts, which are given by Eq. (6) and discussed in Sec. V C.

A. Permanent-dipole interactions

The permanent dipole moment of a Rydberg state with energy $W(E)$ in an electric field E is given by the slope, $-dW(E)/dE$. Therefore, large permanent-dipole interactions are achieved by exciting atoms into Rydberg levels with large slopes in the Stark map. An example of a Stark map for Rb in the vicinity of the $45D$ state is shown in Fig. 9(a). Since in lowest order the energy shifts of the states with linear Stark effect have an upper limit of $\frac{3}{2}En^2$, the magnitude of the permanent dipole moment is limited by $p=\frac{3}{2}n^2$. Following Eq. (1), the magnitude of the dipole-dipole interaction energy is then limited by $4.5n^4/R^3$ (for $\theta=0$), which for $n=45$ and $R=5$ μm exceeds 100 MHz.

In addition to large dipole moments, the utilized Rydberg levels must also have sufficient low-angular-momentum (low-ℓ) character so that selection rules allow for efficient laser excitation from low-lying atomic states. Stark states with maximal dipole moment do not satisfy this requirement. Stark states with both large permanent dipole moment and reasonably high oscillator strength from low-lying atomic states are found in the intersection region between low-ℓ and linear Stark states, as indicated by the circle in Fig. 9(a). For a discussion of the tradeoff between electric dipole moment and oscillator strength see Ref. [32].

Inspecting Eq. (2) and noting that the diagonal matrix element $\langle\lambda,m_j|\otimes\langle\lambda,m_j|V_{dd}|\lambda,m_j\rangle\otimes|\lambda,m_j\rangle$ does not couple different m manifolds, it is immediately apparent that the permanent-dipole shift $\Delta W^{(1)}=p_z^2(1-3\cos^2\theta)/R^3$, where $p_z=-\langle\lambda,m_j|z|\lambda,m_j\rangle$. In Fig. 9(b) we show the permanent-dipole shift at $\theta=0$ of the two-particle state that converges into $2\times|45D_{5/2},m_j=1/2\rangle$ for $E\rightarrow0$ [bold line in Fig. 9(a)]. In the electric-field range $E\lesssim7$ V/cm, the shift is small while the oscillator strength from low-lying P states is large. In the range $7\lesssim E\lesssim9$ V/cm, the shift increases and reaches $\approx90\%$ of the limiting value $-4.5n^{*4}/R^3$ mentioned above, while the oscillator strength from low-lying P-states rapidly drops, as shown in Fig. 9(c). At an electric field of $E\approx8$ V/cm we find both reasonably large permanent-dipole shifts and oscillator strengths. The oscillations seen in Fig. 9(b) for fields $E\gtrsim11$ V/cm reflect corresponding oscillations of the slope (=dipole moment) of the investigated level—the bold line in Fig. 9(a)—in the n-mixing regime.

Generally, it should be possible to employ the electric-field dependence of permanent-dipole Rydberg-Rydberg interactions to enable and disable the Rydberg blockade in a controlled manner. Since this interaction is $\propto[1-3\cos^2(\theta)]$,

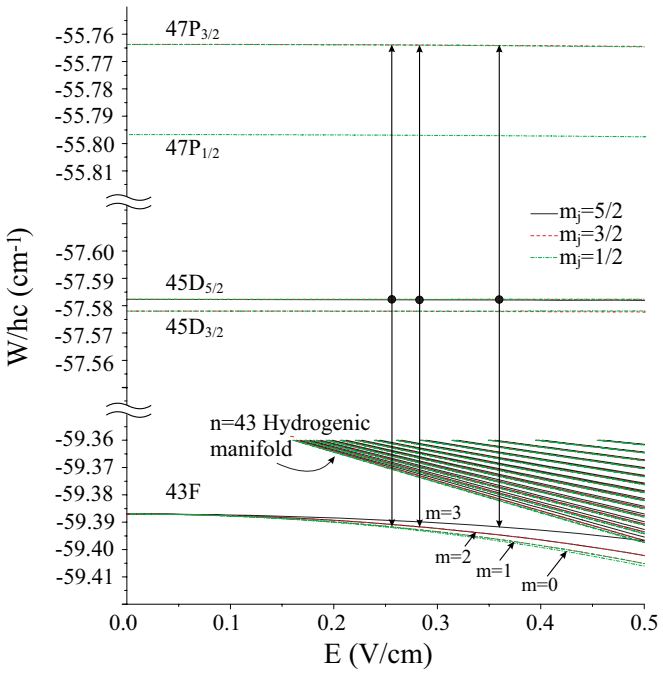

FIG. 10. (Color online) Stark map showing the detailed energy structure of the 45*D*, 47*P*, and 43*F* states. The vertical arrows indicate the resonant transitions corresponding to the interaction channels in Eq. (12).

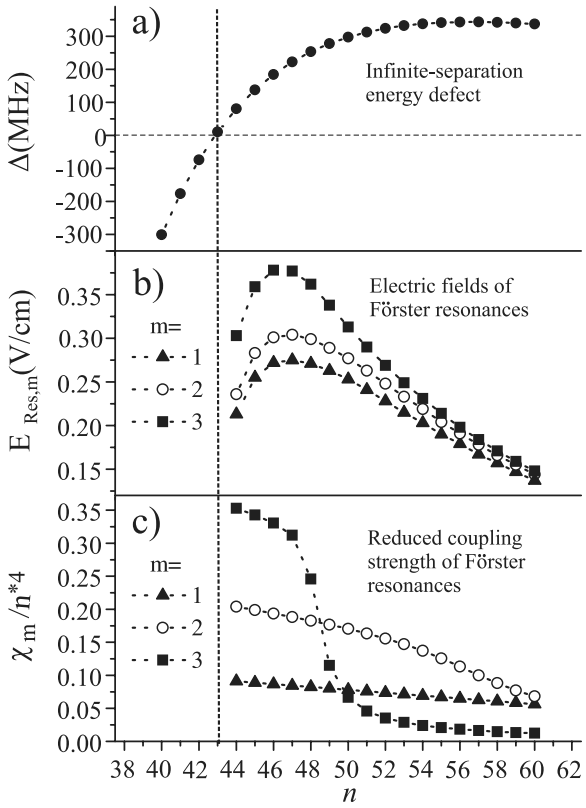

FIG. 11. (a) Infinite-separation energy defects, Δ, of the channel $2\times nD_{5/2}\rightarrow(n-2)F+(n+2)P_{3/2}$ vs n. (b) Electric fields, $E_{\mathrm{Res},m}$ at which the magnetic subchannels identified in Eq. (12) become resonant. (c) Scaled reduced coupling strengths, χ_m/n^{*4}, $m\in\{1,2,3\}$, of the channels in panel (b) vs n.

it is strongly dependent on θ and vanishes at $\theta=55°$. In experiments one may be able to avoid the angle $\theta=55°$ through the use of an optical lattice or an appropriately configured system of miniature atom traps.

B. Förster-resonance interactions

A second method for achieving large interaction energies is to tune Rydberg-Rydberg collisional interactions, such as the ones described in Sec. III, into exact resonance via the application of a relatively weak external electric field [8,15,33], thereby inducing a Förster resonance. For sufficiently large atom-atom distance, the resultant resonant shift dominates any other van der Waals shifts that may also be present. As an example, we consider the channel $2\times nD_{5/2}\rightarrow(n-2)F+(n+2)P_{3/2}$. The electric fields required to tune these interactions into exact resonance are too small to change the angular-momentum-character of the involved P and D states and to break their fine-structure coupling, as illustrated in the example shown in Fig. 10 (upper two panels). As a result, in weak electric fields the P and D states are not significantly perturbed, and we may use electric-field-free quantum numbers (ℓ, j, and m_j) to identify those states. However, the very small fine structure of the involved F state is broken in the electric-field range of interest, as is apparent in the bottom panel of Fig. 10. Therefore, we label the F states by magnetic quantum numbers for electron spin and orbital angular momentum, m_s and m, respectively. (In some cases, even the orbital-angular-momentum character of the involved F state becomes significantly perturbed.)

The detailed coupling scheme of the Förster resonances $2\times nD_{5/2}\rightarrow(n-2)F+(n+2)P_{3/2}$ is most transparent for the case that the initially excited two-atom state is $2\times|nD_{5/2},m_j=5/2\rangle$. In this case, the operator in Eq. (2) allows only the three couplings

$$\begin{aligned}
2\times|nD_{5/2},m_j=5/2\rangle &\rightarrow |(n+2)P_{3/2},m_j=3/2\rangle \\
&\quad +|(n-2)F,m_s=1/2,m=1\rangle,\\
2\times|nD_{5/2},m_j=5/2\rangle &\rightarrow |(n+2)P_{3/2},m_j=3/2\rangle \\
&\quad +|(n-2)F,m_s=1/2,m=2\rangle,\\
2\times|nD_{5/2},m_j=5/2\rangle &\rightarrow |(n+2)P_{3/2},m_j=3/2\rangle \\
&\quad +|(n-2)F,m_s=1/2,m=3\rangle.
\end{aligned} \tag{12}$$

In zero electric field, these couplings have infinite-separation energy defects with magnitudes ranging from 0 to $\sim$400 MHz for $40\leqslant n\leqslant 60$, as shown in Fig. 11(a). In the range $n\geqslant 44$ they can be tuned into resonance by application of electric fields of up to about 0.4 V/cm, which tune the infinite-separation energy defects downward toward negative values. The tuning largely occurs through the Stark shifts of the F levels, which have, due to their small quantum defect, the largest electric polarizabilities among the involved states [$\alpha\approx-2.1$ GHz/(V/cm)^2, -1.7 GHz/(V/cm)^2, and -1.1 GHz/(V/cm)^2 for 43*F*, $m=1,2,3$, respectively].

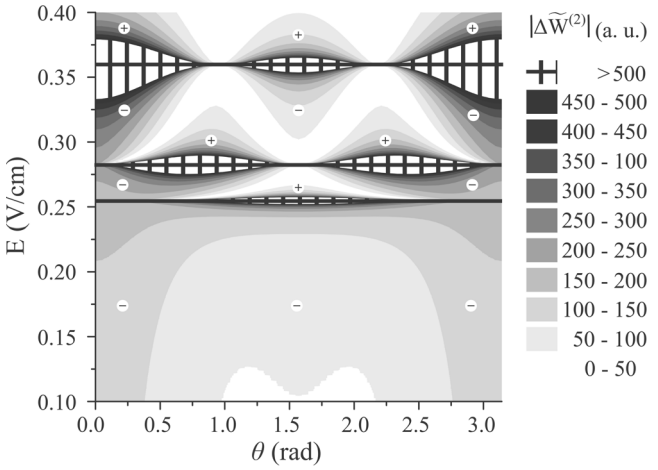

FIG. 12. Scaled energy level shifts, $\Delta\tilde{W}^{(2)}$ of $2\times|45D_{5/2}, m_j=5/2\rangle$ states as a function of θ and the applied electric field. The magnitude of the scaled shifts are shown on the right-hand side and the signs of the shifts are indicated on the figure.

Since the polarizabilities depend on m, the couplings in Eq. (12) come into resonance at slightly different electric fields, as shown in Fig. 11(b). Inspecting Eq. (2) it is seen that the coupling strengths follow angular and radial dependencies $-\frac{3}{2}\chi_1 \sin^2(\theta)/R^3$, $-\frac{3}{\sqrt{2}}\chi_2 \sin(\theta)\cos(\theta)/R^3$, and $\chi_3\left[1-\frac{3}{2}\sin^2(\theta)\right]/R^3$, with reduced coupling strengths χ_m for $m=1,2,3$. In Fig. 11(c) we show the reduced coupling strengths scaled by n^{*4} at the resonant electric fields as a function of n. In the range $44\lesssim n\lesssim 48$, the scaled χ values are fairly constant, reflecting the fact that in this range of n the F states $|(n-2)F, m_s=1/2, m\rangle$ with $m=1,2,3$ are mostly unperturbed. For $n\gtrsim 49$ the state $|(n-2)F, m_s=1/2, m=3\rangle$ becomes increasingly mixed with high-ℓ hydrogenic states, leading to a spread of F character over multiple states and, therefore, to an abrupt drop of the χ value of the strongest resonance (χ_3). The resonances involving $|(n-2)F, m_s=1/2, m=2\rangle$ and $|(n-2)F, m_s=1/2, m=1\rangle$ exhibit similar reductions in strength at somewhat higher values of n.

If one of the subchannels in Eq. (12) is exactly resonant, the resultant level shifts of the two-atom states are first-order and are given by the coupling strength of the resonant channel [see Eq. (5)]. The two-particle states that correspond to the two eigenvalues in Eq. (5) are given by the symmetric and antisymmetric combinations of $2\times|nD_{5/2}, m_j=5/2\rangle$ and $|(n-2)F, m_s=1/2, m\rangle\otimes|(n+2)P_{3/2}, m_j=3/2\rangle$. For instance, at $n=45$, $R=5$ μm, $\theta=0$, and $E=0.36$ V/cm the resonance for $m=3$ generates two such superposition states at energy separations of about ± 18 MHz from the interaction-free energy. In comparison, the van der Waals shift of the state $2\times|45D_{5/2}, m_j=5/2\rangle$ at $E=0$ would only be of the order of 1 MHz. Therefore, strong binary Rydberg-Rydberg interactions may be turned on and off by rapidly tuning interactions of the type in Eq. (12) into and out of resonance by switching weak electric fields. Similar to the permanent-dipole interactions studied in Sec. V A, the Förster-resonance interactions also strongly depend on the angle θ for a given interaction channel. The θ dependence renders the interactions ineffective along certain angles.

C. van der Waals shifts in electric fields

The channels identified in Eq. (12) cause some shifts even if the electric field E does not induce an exact Förster resonance. For sufficiently large separation R, these level shifts can be calculated in second order, as a function of θ and E, using Eq. (6). As an example, in Fig. 12 we plot the level shift of the state $2\times|45D_{5/2}, m_j=5/2\rangle$ as a function of E and θ. In the range $E\lesssim 0.25$ V/cm, the van der Waals shifts are always negative and have a weak dependence on θ. The interaction channels in Eq. (12) generate prominent resonant features that follow angular patterns proportional to $\left[\chi_1\frac{3}{2}\sin^2(\theta)\right]^2$ near 0.255 V/cm, $\propto\left[\chi_2\frac{3}{\sqrt{2}}\sin(\theta)\cos(\theta)\right]^2$ near 0.283 V/cm, and $\propto\left\{\chi_3\left[1-\frac{3}{2}\sin^2(\theta)\right]\right\}^2$ near 0.359 V/cm. [Note that these expressions correspond to the squares of the angular dependencies mentioned in the paragraph after Eq. (12).] For electric fields just below a resonance, the shifts are negative, because the energy defect, Δ, of the nearest-resonant term is >0. For electric fields just above a resonance, the shifts tend to be positive, because the energy defect, Δ, of the nearest-resonant term is <0. In between resonances, the sign of the second-order shift varies as a function of θ due to the competing effects of two nearby resonances with different angular profiles, one producing positive and the other producing negative second-order shifts.

We have investigated in great detail other Förster resonances as well. The resonances of the states $2\times|nD_{5/2}, m_j=3/2\rangle$ and $2\times|nD_{5/2}, m_j=1/2\rangle$ are qualitatively similar to those of the states $2\times|nD_{5/2}, m_j=5/2\rangle$ discussed here, but have more than three allowed angular-momentum subchannels (up to eight) and occur at somewhat different electric fields. Many more Förster resonances occur at fields larger than the ones displayed in Fig. 12. However, due to the increasingly complicated underlying Stark maps, these higher-field Förster resonances follow rather erratic patterns and are usually weak. Therefore, any experimental applications of Förster resonances will likely employ simple cases, such as the ones discussed in this section.

D. Experimental considerations

The control of binary interactions in Rydberg blockade experiments using electric fields of the magnitudes discussed in Sec. V A requires a high degree of temporal and spatial field stability. Variations of Stark shifts due to field instabilities should be less than the laser linewidth (which, in order to observe blockade effects, must be smaller than the binary interaction under investigation). For excitation bandwidth $\delta\nu$, the temporal electric-field variation, δE, should satisfy $p\delta E\lesssim h\delta\nu$. For $\delta\nu=5$ MHz, excitation of atoms into $45D$ states, and assuming a dipole moment p near the upper limit, $p=\frac{3}{2}n^2$, we estimate a required temporal field stability $\delta E\lesssim 0.0015$ V/cm. Furthermore, spatial Stark-shift variations over the range of the excitation blockade and the diameter of the excitation region should both be $\lesssim h\delta\nu$. For $\delta\nu=5$ MHz and $45D$ states, the resultant limitation for the electric-field inhomogeneity is $|\nabla E|\lesssim 1$ V/cm^2. While these requirements on temporal and spatial field stability do not pose enormous experimental problems, they are stringent enough that they

must be taken into account in the design of Rydberg-blockade experiments.

VI. CONCLUSION

We have calculated the van der Waals level shifts, V_{Int}, of pairs of interacting Rb Rydberg atoms in zero applied field for different quantum numbers n, ℓ, j and m_j, taking into account a large number of perturbing states. We have identified states with interaction properties favorable for several applications, including quantum information processing and collision studies in cold Rydberg-atom gases. The calculations were used to analyze data obtained in a recent experiment on the Rydberg blockade. We have also calculated the energy level shifts of Rb Rydberg states for optical excitation in the presence of an applied electric field. We have discussed the calculations in the context of possible schemes which could be used for electric-field control of the blockade. In the future, we also plan to include higher-order multipole interactions in our level shift calculations.

This work suggests several future avenues for experimental research on the Rydberg blockade and on systems of interacting Rydberg atoms in general. We plan to compare the dependence of the Mandel Q-parameter of Rydberg excitation distributions on n for several different types of quantum states ($nD_{5/2}$, $nD_{3/2}$, and $nS_{1/2}$ states). Thereby, the effects of the near-resonant interaction channels $2\times 43D_{5/2}\rightarrow 41F_{7/2}+45P_{3/2}$ and $2\times 58D_{3/2}\rightarrow 56F_{5/2}+60P_{1/2}$ on the Mandel Q-parameter are of particular interest. One may experimentally explore the use of electric fields in controlling the effectiveness of the Rydberg blockade. Specifically, we intend to measure the Mandel Q-parameter to characterize the effectiveness of both the permanent-dipole-interaction method and the Förster-resonance tuning method, described in Secs. V A and V B, respectively. The results presented here may also be used to study the dependence of plasma formation in cold Rydberg gases on various quantum states and excitation geometries.

ACKNOWLEDGMENTS

The authors would like to thank Professor Paul Berman for numerous valuable discussions. This work was supported in part by NSF Grant No. PHY-0114336 and PHY-0555520.

[1] A. Walz-Flannigan, J. R. Guest, J.-H. Choi, and G. Raithel, Phys. Rev. A **69**, 063405 (2004).
[2] W. Li *et al.*, Phys. Rev. A **70**, 042713 (2004).
[3] T. C. Killian, S. Kulin, S. D. Bergeson, L. A. Orozco, C. Orzel, and S. L. Rolston, Phys. Rev. Lett. **83**, 4776 (1999).
[4] M. P. Robinson, B. Laburthe Tolra, Michael W. Noel, T. F. Gallagher, and P. Pillet, Phys. Rev. Lett. **85**, 4466 (2000).
[5] W. Li, P. J. Tanner, and T. F. Gallagher, Phys. Rev. Lett. **94**, 173001 (2005).
[6] F. Robicheaux, J. Phys. B **38**, S333 (2005).
[7] B. Knuffman and G. Raithel, Phys. Rev. A **73**, 020704(R) (2006).
[8] M. D. Lukin, M. Fleischhauer, R. Côté, L. M. Duan, D. Jaksch, J. I. Cirac, and P. Zoller, Phys. Rev. Lett. **87**, 037901 (2001).
[9] D. Jaksch, J. I. Cirac, P. Zoller, S. L. Rolston, R. Côté, and M. D. Lukin, Phys. Rev. Lett. **85**, 2208 (2000).
[10] M. Saffman and T. G. Walker, Phys. Rev. A **66**, 065403 (2002).
[11] I. Bouchoule and K. Mølmer, Phys. Rev. A **65**, 041803(R) (2002).
[12] D. Tong, S. M. Farooqi, J. Stanojevic, S. Krishnan, Y. P. Zhang, R. Côté, E. E. Eyler, and P. L. Gould, Phys. Rev. Lett. **93**, 063001 (2004).
[13] Kilian Singer, Markus Reetz-Lamour, Thomas Amthor, Luis Gustavo Marcassa, and M. Weidemüller, Phys. Rev. Lett. **93**, 163001 (2004).
[14] T. Cubel Liebisch, A. Reinhard, P. R. Berman, and G. Raithel, Phys. Rev. Lett. **95**, 253002 (2005).
[15] Thibault Vogt, Matthieu Viteau, Jianming Zhao, Amodsen Chotia, Daniel Comparat, and Pierre Pillet, Phys. Rev. Lett. **97**, 083003 (2006).
[16] F. Robicheaux and J. V. Hernández, Phys. Rev. A **72**, 063403 (2005).
[17] C. Ates, T. Pohl, T. Pattard, and J. M. Rost, J. Phys. B **39**, L233 (2006).
[18] I. E. Protsenko, G. Reymond, N. Schlosser, and P. Grangier, Phys. Rev. A **65**, 052301 (2002).
[19] M. Saffman and T. G. Walker, Phys. Rev. A **72**, 022347 (2005).
[20] K. Afrousheh, P. Bohlouli-Zanjani, D. Vagale, A. Mugford, M. Fedorov, and J. D. D. Martin, Phys. Rev. Lett. **93**, 233001 (2004).
[21] Marcel Mudrich, Nassim Zahzam, Thibault Vogt, Daniel Comparat, and Pierre Pillet, Phys. Rev. Lett. **95**, 233002 (2005).
[22] S. M. Farooqi *et al.*, Phys. Rev. Lett. **91**, 183002 (2003).
[23] A. L. de Oliveira, M. W. Mancini, V. S. Bagnato, and L. G. Marcassa, Phys. Rev. Lett. **90**, 143002 (2003).
[24] Thomas J. Carroll, Katharine Claringbould, Anne Goodsell, M. J. Lim, and Michael W. Noel, Phys. Rev. Lett. **93**, 153001 (2004).
[25] A. Dalgarno and W. D. Davidson, Adv. At. Mol. Phys. **2**, 1 (1966).
[26] M. Marinescu and A. Dalgarno, Phys. Rev. A **52**, 311 (1995).
[27] M. Marinescu, Phys. Rev. A **56**, 4764 (1997).
[28] Kilian Singer, Jovica Stanojevic, Matthias Weidemüller, and Robin Côté, J. Phys. B **38**, S295 (2005).
[29] A. Schwettmann, J. Crawford, K. R. Overstreet, and J. P. Shaffer, Phys. Rev. A **74**, 020701(R) (2006).
[30] L. Schiff, *Quantum Mechanics* (McGraw-Hill, New York, 1968).
[31] L. Mandel, Opt. Lett. **4**, 205 (1979).
[32] J.-H. Choi, B. Knuffman, T. Cubel Liebisch, A. Reinhard, and G. Raithel, Adv. At., Mol., Opt. Phys. **54**, 131 (2007).
[33] W. R. Anderson, J. R. Veale, and T. F. Gallagher, Phys. Rev. Lett. **80**, 249 (1998).
[34] Wenhui Li, I. Mourachko, M. W. Noel, and T. F. Gallagher, Phys. Rev. A **67**, 052502 (2003).
[35] C. J. Lorenzen and K. Niemax, Phys. Scr. **27**, 300 (1983).
[36] C. E. Moore, *Atomic Energy Levels* NSRDS-NBS 35 (U.S. GPO, Washington, DC, 1971).
[37] The lowest Q values we have measured are -0.15 ± 0.05.